Pharmaceutical Sciences and Drug Design
ISSN: 3062-4428
2026, Volume 6, Issue 1, Page No: 249-265

Available online at: www.galaxypub.co/page/journals

Galaxy Publication

Galaxy Publication

Engineered Silver Carbonate Nanoparticles with Dual Antibacterial and Tissue-Regenerative Properties

Ahmed El-Kholy[1]*, Nour Abdelrahman[1], Karim Hassan[2]

[1]Department of Pharmaceutical Sciences and Drug Engineering, Faculty of Pharmacy, Alexandria University, Alexandria, Egypt.
[2]Department of Medicinal Chemistry and Drug Development, Faculty of Medicine, Ain Shams University, Cairo, Egypt.

***E-mail** ✉ ahmed.elkholy@outlook.com

Received: 28 February 2026; **Revised:** 20 May 2026; **Accepted:** 23 Mau 2026

ABSTRACT

Metal-derived nanoparticles have attracted interest for numerous medical applications due to their functional, physical, and chemical properties, including their ability to fight bacteria, reduce inflammation, and support tissue regeneration. This investigation sought to determine the curative capacity of novel silver carbonate nanostructures to facilitate wound closure and their antibacterial activity against *Pseudomonas chengduensis* and *Staphylococcus aureus*. For this research, Ag2CO3 nanoparticles were produced via a dual-stage procedure intended to enhance the substance's biomedical function and biological safety. Hemolytic activity assays on blood drawn from a healthy adult male donor were performed to characterize the manufactured NPs and establish their compatibility with living systems. In addition, molecular docking simulations were performed to validate the binding of silver NPs to biological macromolecules. Specifically, the manufactured NPs induced hemolysis below 5% at multiple tested concentrations, verifying their suitability for clinical use. The NPs also displayed positive metabolic regulation; they boosted T3/T4 hormone concentrations and produced a beneficial effect on Insulin-like Growth Factor 1 (IGF-1) in diabetic experimental subjects. They likewise accelerated the repair timeline, with the diabetic injuries reaching complete re-epithelialization by day 13, whereas the untreated counterparts reached the same endpoint only by day 16. The manufactured Ag2CO3 NPs exhibited strong antimicrobial activity against both *Pseudomonas chengduensis* and *Staphylococcus aureus*, suggesting they are a viable candidate for managing infections in biomedical tissue engineering applications. The outcomes reveal that innovative production routes yield NPs with greater therapeutic potential; however, further exploration of their metaphysical and hormonal effects is needed.

Keywords: Ag2CO3 nanoparticles, Biocompatibility, Metabolic effects, Insulin, Molecular docking

How to Cite This Article: El-Kholy A, Abdelrahman N, Hassan K. Engineered Silver Carbonate Nanoparticles with Dual Antibacterial and Tissue-Regenerative Properties. Pharm Sci Drug Des. 2026;6(1):249-65. https://doi.org/10.51847/qxh9XnwaC2

Introduction

Across the range of metallic nanostructures, silver has received thorough examination in the last few years, mainly for its appealing physical and chemical properties, which are recognized as well-suited for a variety of purposes, especially in cleansing water and air, as well as in medical applications. These nanosized materials exhibit a high surface-to-volume ratio and, correspondingly, greater reactivity, which amplifies their catalytic and antimicrobial abilities. Among the available fabrication strategies, chemical reduction techniques stand out as efficient for generating silver nanostructures with controlled nanoscale geometries and dimensions [1]. Such an approach provides strong control over the production process, thereby yielding nanostructures that exhibit robust functionality across multiple settings [2].

Silver nanostructures also have significant potential in the medical field, including injury repair, metabolic modulation, and pathogen suppression. The bactericidal properties of AgNPs are well established, as they target

Gram-positive, Gram-negative, fungal, and viral infectious agents. Such properties make silver nanostructures indispensable for thwarting infections and treating wounds [3]. These nanostructures feature enlarged surface areas that enable more efficient interaction with microbial organisms, thereby enhancing their antimicrobial activity [4]. Furthermore, they exhibit biological compatibility, promote cellular proliferation, and facilitate tissue reconstruction, thereby shortening recovery periods [5].

The wound-healing capabilities of silver nanostructures are believed to arise from their ability to reduce inflammation and promote collagen formation. This phenomenon is linked to the release of silver ions, which are known to have both germicidal and anti-inflammatory effects, particularly when incorporated into hydrogels or other wound dressings [6]. Such prolonged liberation is extremely valuable in the management of persistent sores, and silver-nanoparticle-loaded formulations have been developed to deliver therapeutic agents gradually over extended periods. Studies have shown that embedding silver nanoparticles into bandaging materials enhances their performance, especially in treating diabetic ulcers and thermal injuries [7].

A further promising use of silver nanostructures in healthcare relates to the control of metabolic function. These nanomaterials can beneficially influence cellular metabolism, which is advantageous for medical interventions. For example, silver nanoparticles have been shown to modulate levels of oxidative stress and inflammatory responses within cells, making them useful for tackling wound-related infections and related biomedical challenges [8]. Adjusting cellular metabolic mechanisms via silver nanostructures lays the groundwork for tailored medical therapies and enhanced treatment results [9]. Furthermore, chemical reduction processes used to generate silver nanostructures enhance their ecological and medical potential while advancing sustainable development [10]. Such methods use appropriate reagents to convert Ag ions into Ag NPs, yielding superior-quality nanostructures with consistent attributes [11]. Thanks to their enhanced activity and biological tolerance, chemically produced silver nanostructures have potential applications across many industries [12].

Despite the many prospects, certain hurdles remain in deploying silver nanostructures in ecological and medical contexts. For instance, the risk of biological buildup and harmful effects on non-target organisms, along with issues regarding nanomaterial durability across diverse environments and the need for long-term research, remain relevant [13]. Overcoming these barriers will require cooperation across materials chemistry, toxicity assessment, and ecological studies, as well as breakthroughs in the generation of secure and favorable silver nanostructures [14].

The growing need for solutions to ecological contamination and the ongoing search for more effective biomedical treatments underscore the importance of this undertaking. The goal of the current study is to manufacture silver nanostructures via a chemical reduction route and to gauge their catalytic activity in degrading methylene blue dye and agricultural chemical residues, as well as their wound-healing, metabolic-regulation, and microbe-inhibition traits. This inquiry is significant because it may contribute to the development of eco-conscious techniques for pollution mitigation and to the development of successful clinical strategies for wound and infection care. Broadening insight into chemically fabricated silver nanostructures through this research will foster scientific advancement that benefits the wider population.

Materials and Methods

Research design

The experimental blueprint of the present work was laid out in a stepwise fashion, centering on the production of silver carbonate nanostructures (Ag2CO3-NS) through a managed chemical reduction pathway, and their subsequent examination via XRD, SEM, and FTIR to corroborate their chemical architecture, physical form, and functional traits, in that order. The bactericidal activity of Ag2CO3-NS was assessed in vitro against multiple disease-causing bacterial species. Thereafter, the in vivo arm of the study was conducted in albino mice to determine the metabolic effects of the nanostructures, focusing on blood glucose levels, lipid profiles, and overall physiological condition.

Synthesis and characterization

Silver nanostructures were generated by means of a wet-chemical reduction route taken from the protocol of Umar *et al*. [15]. The starting silver source was silver nitrate (Sigma Aldrich; Lot# SZBF1070V; Darmstadt, Germany), while sodium borohydride (Sigma Aldrich; Darmstadt, Germany) acted as the electron donor. Two distinct reaction environments were maintained to yield two variants of nanostructures. The as-obtained nanoparticles

were then characterized by X-ray diffraction (Bruker D8 Advanced, Karlsruhe, Germany) and scanning electron microscopy. These methods are well-suited for establishing the dimensions, contour, crystallinity, and exterior topology of the nanostructures.

Synthesis

The fabrication of 20 mM Ag2CO3 NPs was executed via a dual-stage sequence derived from Umar *et al*. [15]. To begin, 15 mL of 20 mM AgNO3 solution was blended with high-grade AgNO3 powder in approximately 15 mL of deionized water, with constant agitation until a faintly gleaming, see-through liquid formed. Next, 10 mL of 20 mM Na2CO3 (Sigma-Aldrich; Darmstadt, Germany) solution was added dropwise to the earlier mixture, prompting the formation of a silver carbonate sediment. This incremental dispensing enabled a gradual, regulated buildup of silver carbonate, favoring uniform nucleation of nanoscale particles.

Upon finishing the Na2CO3 delivery, the anionic reducer NaBH4 (Sigma Aldrich; Darmstadt, Germany) was brought into the mix. This phase triggered the reduction cascade, leading to the formation of silver carbonate nanoparticles within 10 min. Nonetheless, to safeguard nanoparticle stability, an additional 20 min of stirring was required. Throughout this window, as the particles began to enlarge, they converged on a stable dimension and morphology, thereby circumventing clustering.

Once nanoparticle genesis was complete, the colloidal suspension was spun at 10,000 rpm for 15 min to remove the nanoparticles from the reaction liquor. The overlying fluid was poured off, and the compacted nanoparticle mass was repeatedly flushed with deionized water to remove lingering residues of the initial reagents or unintended byproducts generated during the operation. After rinsing, the nanoparticles were dried down to produce the final powdered form of silver carbonate nanoparticles, which were subsequently used for characterization analyses.

Characterization

Following the generation of silver carbonate nanoparticles (Ag2CO3 NPs), a range of characterization methods was used to assess their physicochemical and structural properties comprehensively.

Fourier transform infrared spectroscopy (FT-IR; Cary630, Agilent Technologies, Santa Clara, CA, USA): The bonding configurations and functional chemical groups housed within the synthesized nanoparticles were decoded with the assistance of FT-IR spectroscopy. Spectra were collected over 4000-400 cm−1, aiming to detect the carbonate functional group, CO_3^{-}, and to substantiate the formation of Ag2CO3. The distinctive absorption features attributable to carbonate ions were captured, shedding light on the coordination environment and chemical nature of the nanoparticles.

X-ray diffraction (XRD): Crystallographic analysis was performed to determine the crystalline framework, phase identity, and mean domain size of the as-produced Ag2CO3 NPs. Measurements were conducted with a Cu-Kα X-ray beam (λ = 1.5406 Å) scanning a 2θ window of 10–80. The acquired diffractogram was cross-referenced against standard library patterns to authenticate the emergence of the targeted silver carbonate phase. Peak width analysis, in combination with the Scherrer equation, was used to determine the average crystallite size of the generated nanoparticles.

Scanning electron microscopy (SEM): Inspection of external morphology and interparticle arrangement was performed via SEM (JSM-IT100; JEOL Ltd., Tokyo, Japan). High-magnification SEM micrographs supplied granular insight into the particles, encompassing their geometry, surface roughness, and propensity to cluster. The SEM findings buttressed the earlier interpretation and deduction that the fabricated nanoparticles were evenly scattered, manifested nearly uniform particle sizing, and generally adopted spherical or non-uniform shapes.

Research animals

Albino mice were utilized as the model animal system. Vigorous mature albino mice (n = 18–20), with a mean age of 8 ± 1 week and a mean body mass of 30 ± 5 g, were obtained from the Animal House, University of Punjab, Lahore, Pakistan. The mice were accommodated under tightly regulated atmospheric parameters, covering both thermal and moisture levels, within polycarbonate enclosures (temperature: 25.2 °C, humidity: 55%, and light/dark cycles: 12 h). A conventional pelleted feed formulation delivering 21% protein, 48.8% carbohydrate, and 3% fat was provided to the animals. A one-week habituation period was allowed before initiating the experimental procedures. All experimental work took place at the Animal House, Department of Zoology, University of Okara.

Diabetes induction

Hyperglycemia was triggered in albino mice via alloxan, a diabetogenic substance noted for its selective toxicity toward insulin-secreting pancreatic beta cells. A solitary intraperitoneal bolus of alloxan at 150 mg/kg was administered to the mice, triggering a cascade of reactive oxygen intermediate formation that inflicted oxidative injury and beta cell destruction. The outcome was a profound collapse in insulin secretion, giving rise to pronounced hyperglycemia that closely recapitulated the phenotype of type 1 diabetes. The establishment of this diabetic milieu enabled deeper exploration of the mechanistic underpinnings of diabetes and the appraisal of candidate remedies.

Blood sampling and euthanasia procedure

Blood draws from albino mice were executed through a minimally disruptive technique to preserve animal comfort. Several anatomical sites are viable for phlebotomy in albino mice [16], among them the lateral tail vein [17], the saphenous vein [18], the retroorbital sinus, and the cardiac puncture route. For the present study, samples were harvested from the lateral tail vein due to its ease of access and the comparatively modest stress response it elicits in mice. Gentle warming was applied to the vein just ahead of collection to encourage vasodilation and permit withdrawal of the desired volume [15]. To prevent coagulation and extraneous contamination, blood was collected strictly for downstream metabolic profiling. By the close of the experiment, no animal fatalities had occurred.

Metabolic evaluation

Systemic concentrations of T3, T4, TSH, and insulin were determined through Enzyme-linked Immunosorbent Assay (ELISA) kits (Sigma-Aldrich (Merck) Darmstadt, Germany). The hormonal readouts were subsequently juxtaposed between the treated subsets and the untreated control to evaluate the metabolic ramifications of the intervention. Intergroup hormone values were compared to determine whether the differences were statistically significant.

Hemolysis

The hemolytic assay employed whole blood from a 27-year-old male with B-positive blood group status. The specimen was drawn directly into EDTA-coated receptacles to block the clotting cascade. Erythrocytes (RBCs) were isolated by triple rinsing with phosphate-buffered saline (PBS) and centrifugation at 1500 rpm for 5 min after each wash. The pelleted RBCs were thereafter resuspended in PBS to generate a 2% erythrocyte mixture. For hemolysis testing, 100 µL of the RBC preparation was pipetted into test vessels already loaded with 100 µL of either the test article, distilled water (positive control), or PBS (negative control). The admixtures were incubated at 37 °C for 1 h. On completion of incubation, the vessels were centrifuged once more to compact any residual intact cells, and the clear overlying liquid was aspirated. The extent of hemolysis was quantified by measuring the absorbance of the supernatant at 540 nm. Percent hemolysis was derived by normalizing the absorbance readings of the experimental specimens against those of the positive and negative benchmarks. This sequence of steps permitted the determination of the hemolytic liability that the tested materials pose toward human red cells.

$$\text{Percent Hemolysis} = \left(\frac{\text{Absorbance of sample} - \text{Absorbance of negative control}}{\text{Absorbance of positive control} - \text{Absorbance of negative control}}\right) \times 100 \quad (1)$$

Wound healing

To characterize the wound-repair potential of the NPs, a pair of full-thickness standardized punch biopsy wounds (each 1 cm2) was fashioned on the shaved dorsal skin of each albino mouse. The cohort was split into two arms: a control arm receiving saline and an experimental arm receiving silver nanostructures. The nanostructure formulation was directly applied to the lesion sites once daily. The progression of wound closure was tracked and documented through serial digital photography. For the calculation of closure kinetics, wound dimensions were serially recorded at predetermined time points [19].

Antimicrobial activity

The potency of the as-prepared silver nanostructures toward pathogenic bacterial isolates, namely *S. aureus* and *Escherichia coli*, was concurrently examined. The agar well-diffusion protocol was adopted: bacterial suspensions were uniformly spread on agar surfaces, and cylindrical wells were bored to receive the nanostructure aliquots. The inoculated plates were incubated at 37 °C for 24 h, after which the diameter of the transparent inhibitory halo surrounding each well was measured to gauge the presumptive antimicrobial effect.

Docking study

Two protein targets were enrolled in the molecular docking campaign: thyroxine-binding protein (PDB ID: 2CEO), an entity implicated in metabolic governance, and thymidylate kinase (PDB ID: 4GQQ), a participant in antimicrobial mechanisms. Both macromolecular structures were prepared using the Protein Preparation Wizard embedded in the Maestro 12.5 computational suite. The steps included importing the crystallographic coordinates, verifying bond topologies, appending hydrogen atoms, and correcting missing side chains and loop stretches using the Prime module. Hydrogen bonding networks were subsequently optimized, and a full-scale geometric relaxation was executed under the OPLS3e force field. Crystallographic water molecules not mediating direct contacts with ligands were removed.

Ligand construction was undertaken within the LigPrep module of Maestro, incorporating geometric refinement and energy minimization, along with the enumeration of plausible tautomeric forms and ionization states over a pH window of 7.0 ± 2.0. The conformers advanced to docking were those populating the lowest-energy basins of the conformational space. Receptor grids were custom-built for each protein through the Receptor Grid Generation facility. These grids demarcate the search volume and thus direct ligand placement into the designated active site. For 2CEO, the grid was centered on the thyroxine-binding locus; for 4GQQ, it was anchored at the thymidylate kinase catalytic pocket. Van der Waals radii scaling was applied to all nonpolar atoms to grant additional steric tolerance within the docking arena.

Ligand placement into the prepared grids was performed using the Glide docking module in Maestro. Depending on the required sampling depth, either single-precision (SP) or extended-precision (XP) modes were used. The docking engine employed flexible ligand sampling, enabling extensive exploration of conformational variants. The pose ranking relied on the Glide Score, a composite metric that combines hydrogen-bond contributions, hydrophobic burial, and shape matching. Only the uppermost-ranked ligand–receptor configurations were carried forward for detailed inspection.

Protein–ligand contact patterns and interaction energies were next deconvoluted; evaluations encompassed hydrogen bonding, π- π stacking, and hydrophobic packing. For each docked entity, multiple alternative poses were evaluated to determine the most credible binding orientation. Finally, the docked complexes were collated and graphically rendered within Discovery Studio (BIOVIA Discovery Studio Client 2024). The visualization toolkit in Discovery Studio was leveraged to craft high-resolution 2D and 3D portrayals that capture the interplay between ligand atoms and protein-residue environments, including hydrogen-bond networks, hydrophobic enclosures, and π- π stacking configurations. Visual inspection and diagrammatic representation proved instrumental in interpreting and substantiating the docking-derived conclusions [20].

Statistical analysis

The entire experimental dataset was processed using statistical software (GraphPad Prism v10). Results were condensed and displayed as mean ± standard deviation (SD) for each measured variable. Intergroup comparisons between the control and treatment arms were conducted via one-way analysis of variance (ANOVA). A p-value falling below the conventional threshold of 0.05 was regarded as statistically meaningful.

Results and Discussion

Synthesis and characterization

A chemical reduction route was employed to fabricate the Ag2CO3 nanoparticles. SEM, FTIR, and XRD were used to characterize the NPs. SEM imaging indicated that the Ag2CO3 nanoparticles exhibit an irregular, clustered architecture with a coarse, uneven surface morphology. The particles exhibit size heterogeneity and appear to merge into aggregates, suggesting agglomeration. The most striking difference, however, lies in the surface coarseness, which may bear on the substance's reactivity or prospective uses. A morphology of this type suggests

a non-homogeneous formation process, a hallmark of many nanoparticle production methods **(Figure 1).** The synthesized NPs measured 10.29 nm in size **(Figure 2).**

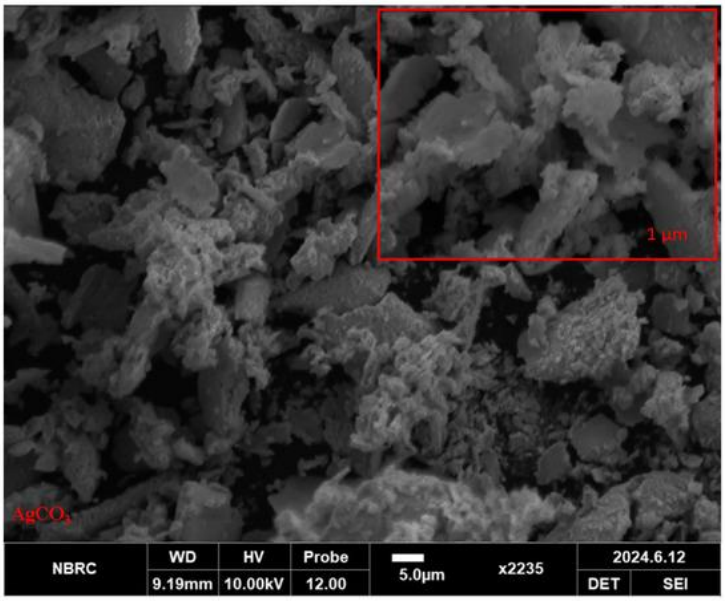

Figure 1. SEM analysis of Ag2CO3 nanoparticles.

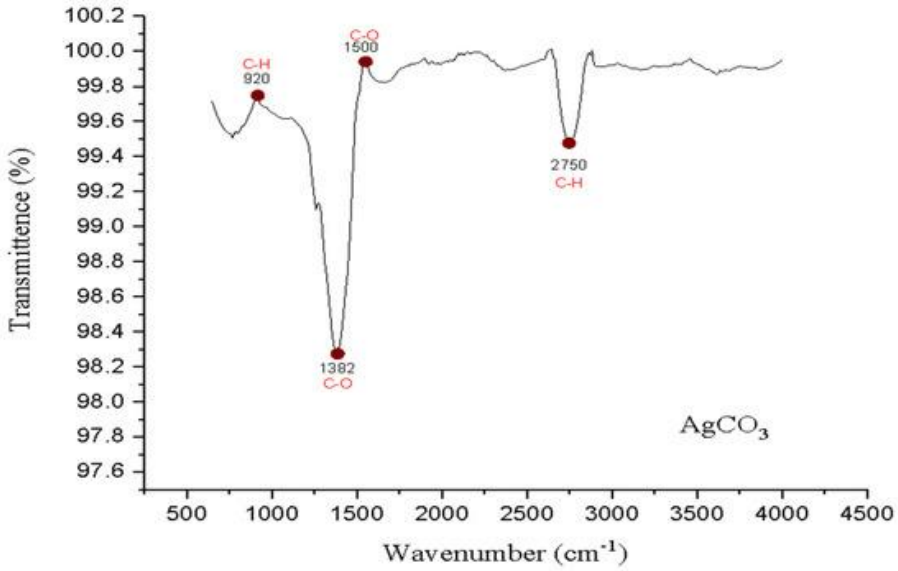

Figure 2. FTIR analysis of Ag2CO3 nanoparticles.

In this study, the FTIR spectrum of Ag2CO3 nanoparticles showed signals indicative of specific functional groups. The prominent, distinctive signals at 1382 cm−1 and 1500 cm−1 are attributed to C-O stretching from the carbonate unit. The signal at 920 cm−1 corresponds to C-H bending, while the one at 2750 cm−1 corresponds to C-H stretching, suggesting the presence of organic traces or surface alterations. These signals also highlight the presence of carbonate groups and other functional groups within the Ag2CO3 nanoparticles, corroborating the particles' chemical constitution and structural arrangement. Functional groups are denoted in red on the marked signals, indicating the functional entity associated with each signal **(Figure 2).**

The X-ray diffractogram of Ag2CO3 nanoparticles shows a series of strong, well-defined peaks, confirming the material's crystalline character. The diffraction signals observed at specific 2θ angles, manifesting as high-intensity features, correspond to distinct crystal planes of Ag2CO3. The enhanced intensity and sharpness of these peaks indicate elevated crystallinity; they reveal the material's intrinsic properties and applications **(Figure 3).**

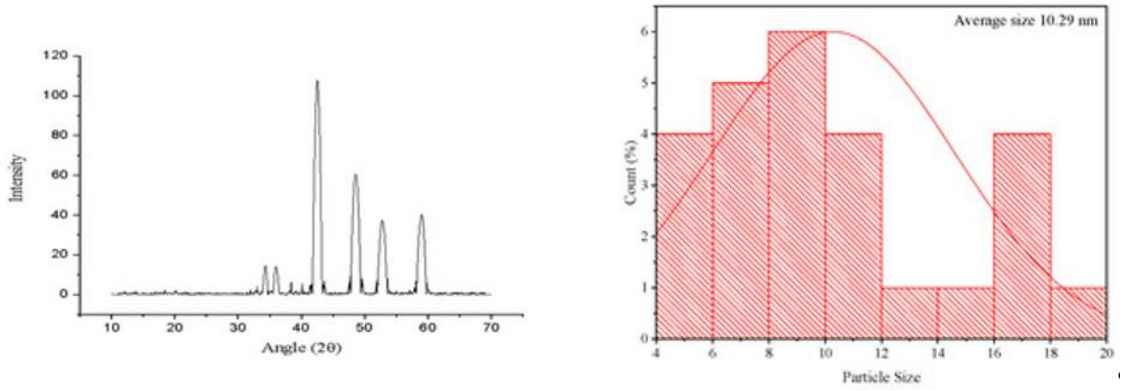

a) b)

Figure 3. XRD analysis (left side) and histogram for the NPs size (right side) of Ag2CO3 nanoparticles.

Biocompatibility

Evaluation of biocompatibility through hemolytic testing uncovered a dose-responsive hemolysis pattern in RBCs exposed to Ag2CO3 nanoparticles. At a concentration of 75 µg/mL, a hemolysis rate of 3.37% was documented. In such assessments, hemolysis percentages falling below 5% are usually taken to reflect favorable biocompatibility [21]. Consequently, one may deduce that the Ag2CO3 NPs qualify as biocompatible with respect to the preservation of erythrocyte membrane integrity across multiple doses. This modest degree of hemolysis supports the deployment of these nanoparticles in biomedical contexts and indicates that they are unlikely to pose a substantial hemolytic toxicity risk in living systems. The observation is relevant to the safe adoption of Ag2CO3 NPs in either therapeutic or diagnostic roles **(Table 1).**

Table 1. Hemolytic activity of different concentrations of Ag2CO3 NPs.

Sr No	Concentration (µg/mL)	P-value	F-value	Hemolysis %
1	25	< 0.0001 ***	408.8	2.55 ± 0.041
2	50			2.98 ± 0.033
3	75			3.37 ± 0.035

= Highly significant.

Metabolic effects

Findings from the metabolic examinations revealed that Ag2CO3 nanoparticles can shift the metabolic landscape of diabetic albino mice in a dose-dependent manner. The higher NP dosage (50 mg/kg) led to a pronounced elevation in T3, T4, TSH, and insulin levels, suggesting a stimulatory effect of Ag2CO3 on thyroid hormone production—an effect absent at the lower dosage. In this way, the investigation sheds light on the intricate association between Ag2CO3 NPs and endocrine regulation, emphasizing the need to determine whether these NPs exert therapeutic or detrimental effects in diabetic states **(Figure 4).**

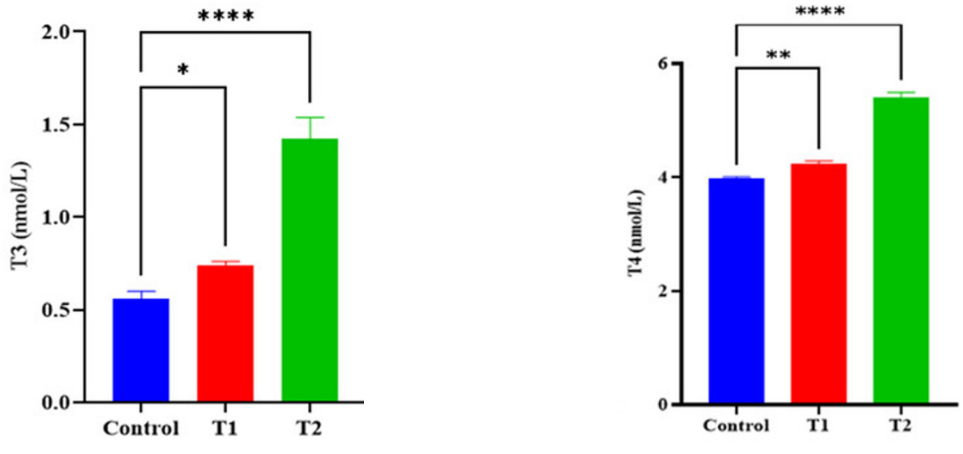

a) b)

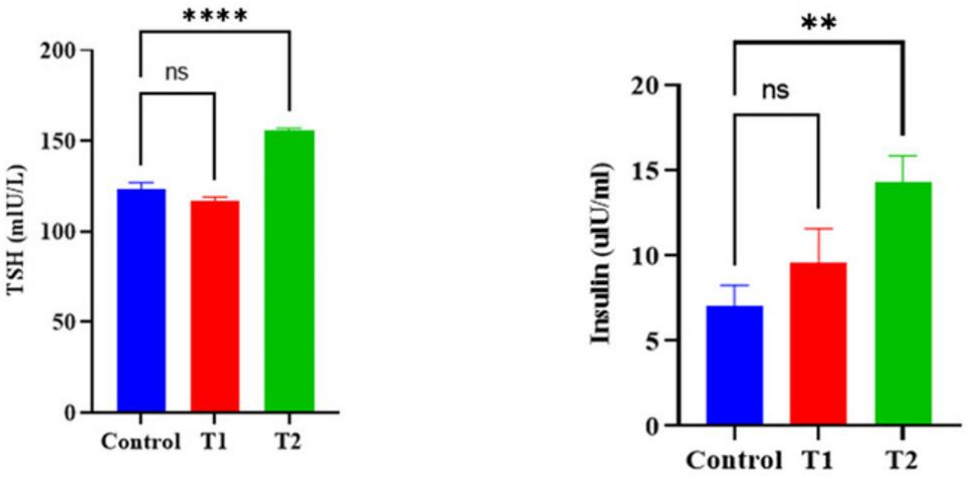

c) d)

Figure 4. Effect of Ag2CO3 nanoparticles on the metabolic profile of diabetic albino mice. P < 0.05—indicates a significant difference, P < 0.01—indicates a very significant difference, P < 0.0001—indicates an extremely significant difference, and ns: P > 0.05—indicates a non-significant difference.

Wound healing

The data demonstrate that lesions treated with Ag2CO3 nanoparticles progress through the healing cascade at a considerably accelerated pace compared with untreated counterparts. Commencing on day 2, the treated lesions undergo more rapid contraction in wound dimensions, with the repair tempo picking up noticeably from day 5 onward. By day 12, the treated lesions are on the verge of full closure, and total restoration is achieved by day 13. In comparison, the untreated group continues to exhibit a steady wound-shrinkage trajectory, achieving complete closure only on day 16. These observations imply that Ag2CO3 nanoparticles powerfully expedite wound repair under diabetic conditions, a phenomenon potentially attributable to their antimicrobial properties and their capacity to support tissue repair. Quicker healing within the treated cohort underscores the potential therapeutic benefits of Ag2CO3 NPs in treating diabetic lesions, which are traditionally difficult to treat owing to disrupted repair pathways in diabetic subjects **(Figures 5 and 6)**.

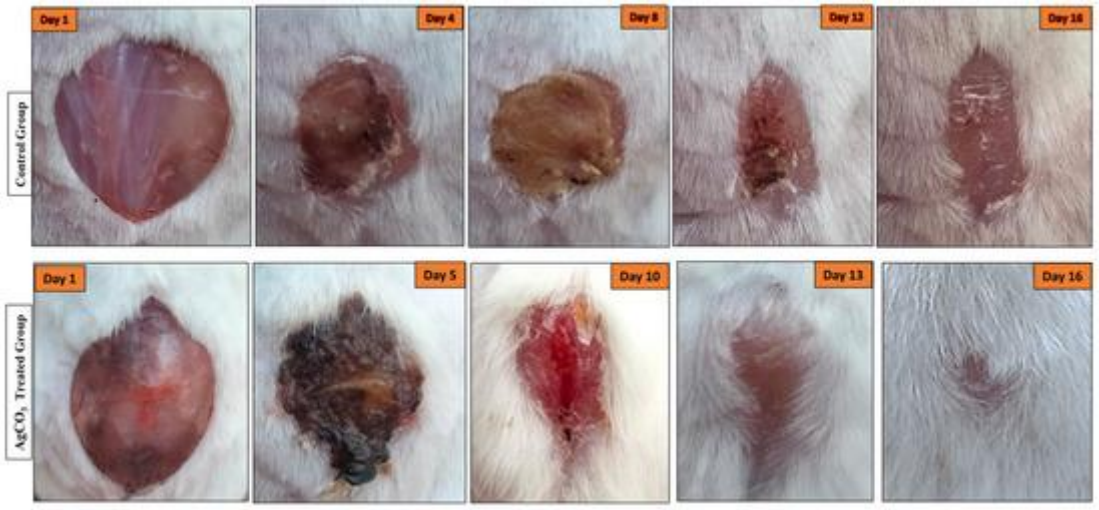

Figure 5. Comparison of wound healing progress between control and Ag2CO3-nanoparticle-treated diabetic wounds.

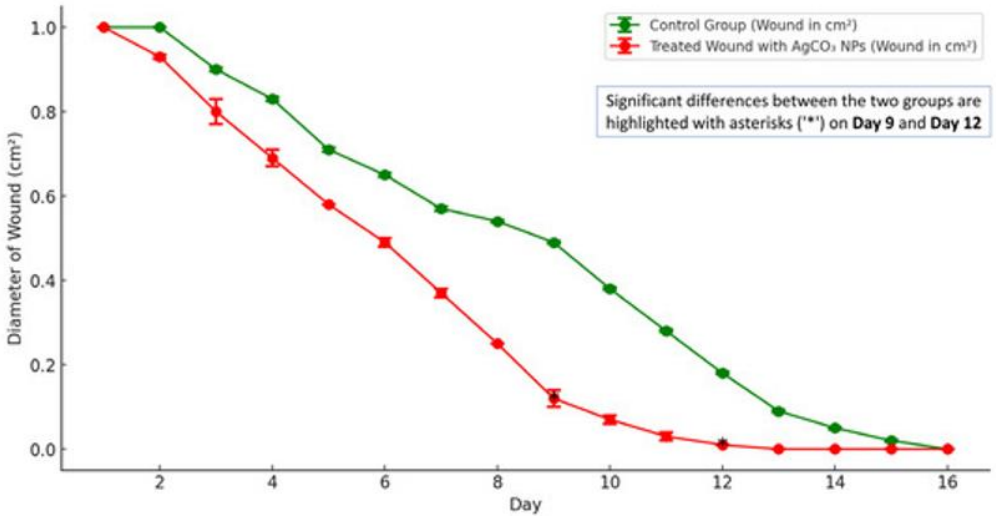

a)

Day	Control Mean	Control STD	Treated Mean	Treated STD	Day	Control Mean	Control STD	Treated Mean	Treated STD
1	1.000	0.000	1.000	0.000	9	0.492	0.002	0.130	0.014
2	1.000	0.000	0.935	0.007	10	0.382	0.002	0.065	0.007
3	0.903	0.004	0.815	0.021	11	0.282	0.002	0.025	0.007
4	0.833	0.004	0.700	0.014	12	0.182	0.002	0.010	0.000
5	0.712	0.004	0.580	0.000	13	0.092	0.002		
6	0.653	0.004	0.500	0.014	14	0.052	0.002	Healed	Healed
7	0.573	0.004	0.375	0.007	15	0.022	0.002		
8	0.542	0.002	0.250	0.000	16	Healed	Healed		

b)

Figure 6. Graphical representation of wound healing progress between control and Ag2CO3-nanoparticle-treated diabetic wounds.

Antimicrobial activity

Based on the collected data, a 1 mg/mL Ag2CO3 preparation exhibits bacteriostatic activity against both *Pseudomonas chengduensis* and *Staphylococcus aureus*, as reflected by an increase in the inhibition zone with increasing test volumes. *P. chengduensis* registers greater sensitivity to Ag2CO3 at the smaller applied volumes (25 µL and 50 µL), as indicated by broader inhibition zones under these reduced quantities. That being said, the inhibition at 75 µL and 100 µL is comparable, and it can be hypothesized that increasing the volume promotes stronger inhibition of both microbes by Ag2CO3 due to the compound's enhanced antimicrobial activity. These observations indicate that Ag2CO3 exhibits broad-spectrum antimicrobial activity, with a slight tendency toward greater efficacy against *P. chengduensis* at elevated concentrations **(Table 2; Figure 7).**

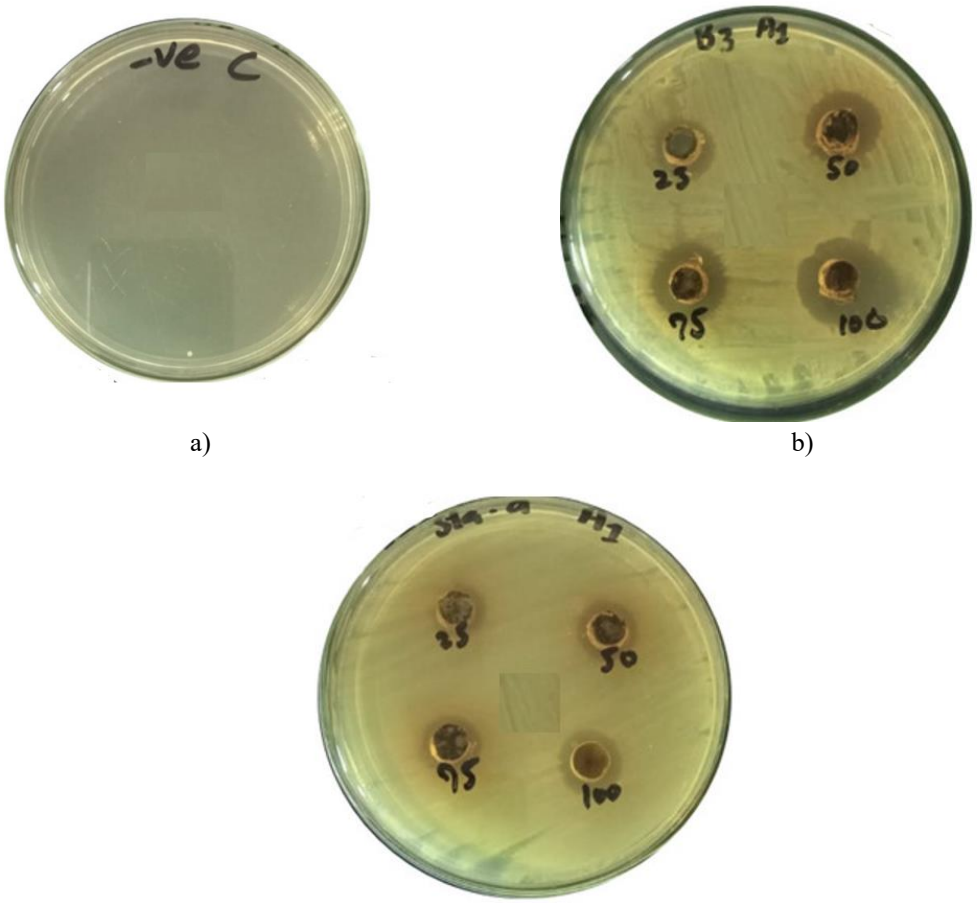

Figure 7. Antimicrobial activity of Ag2CO3 nanoparticle against different bacterial strains: (a) Control; (b) *Pseudomonas chengduensis*; and (c) *Staphylococcus aureus*.

Table 2. Antimicrobial activity (zone of inhibition) of Ag NPs.

Applied volume (µL)	Inhibition zone against *Staphylococcus aureus* (mm)	Inhibition zone against *Pseudomonas chengduensis* (mm)	P-value	t-value
25 µL	4.375 ± 0.38	6.52 ± 0.49	0.0341 *	18.65
50 µL	5.865 ± 0.27	7.255 ± 0.19	0.2035	3.022
75 µL	7.76 ± 0.26	7.86 ± 0.26	0.0303 *	21.0
100 µL	8.175 ± 0.275	8.405 ± 0.29	0.0277 *	23.0

P < 0.05—indicates a significant difference.

Validation of Ag2CO3 engagement with biological proteins linked to metabolic regulation and antimicrobial action through molecular docking simulations

Molecular interaction between Ag2CO3 and thyroxine (T4) (PDB: 2CEO)

The molecular docking assessment detailed here highlights the binding patterns between Ag2CO3 and the thyroxine transporter protein (PDB). The study designated this gene target as 2CEO, a molecule known for its pivotal role in metabolic control. The left-hand panels provide two-dimensional views of how Ag2CO3 interacts with the principal amino acid side chains that govern thyroxine attachment. Green-colored residues—ALA256, ILE198, LEU261, PHE258, and TYR262—denote constructive van der Waals contacts, which are fundamental for securing the ligand inside the binding region and thus imply a capacity to influence metabolic tempo. In contrast, residues tinted in red (ARG260, GLU259, and PHE165) mark zones of steric tension or spatial friction, characterized as "unfavorable bumps" or "clashes" that may undercut the anchoring strength of Ag2CO3.

The three-dimensional model on the right maps the precise spatial disposition of Ag2CO3 within the docking cleft. Red dashed connectors pinpoint disadvantageous close encounters, notably with Arg260, Glu259, and Phe165. Such steric conflicts could suggest that achieving a more favorable fit for Ag2CO3 may require molecular

refinements, enabling the compound to adopt a more functionally relevant orientation for protein engagement. The captured Glide XP GScore of −3.52 points to a moderate tier of binding affinity, underscoring that, although a steady complex can form with the thyroxine-carrying protein, there remains latitude for optimizing the interaction. Because thyroxine orchestrates metabolic cascades and Ag2CO3 lodges within the docking pocket, it stands to perturb the protein's architecture or conformational adaptability, thereby interfering with its duty in setting metabolic pace. Ag2CO3 might either amplify or dampen selected metabolic regulatory functions of thyroxine, contingent on the net shift in global protein conformation and function induced by ligand association **(Figure 8).**

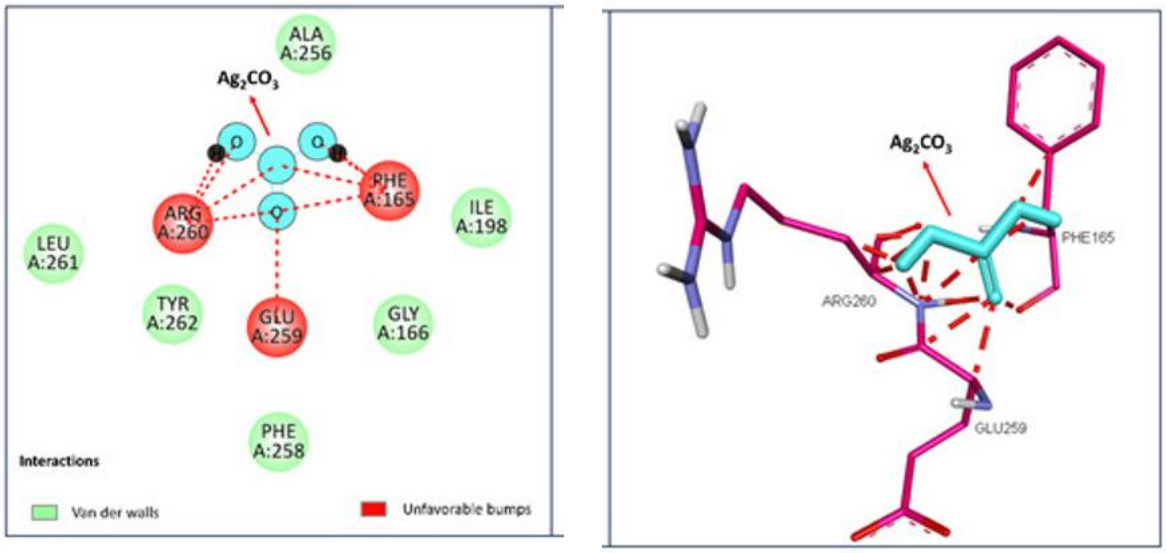

a) b)

Figure 8. Molecular docking analysis of Ag2CO3 with thyroxine-binding protein (PDB: 2CEO): the left panel shows 2D interactions, while the right panel displays the 3D binding pose.

Figure 9 presents an iMODS corroboration panel linked to the docking output, focusing on the protein–ligand motional dynamics. The application of normal mode analysis in this work is supported by the vector arrows in the upper-left schematic, which chart the directional tendencies of protein motion. Such representation helps conceptualize the protein's structural pliability throughout the binding event. The deformability tracing, located at the lower left, flags protein segments amenable to conformational shifts, as indicated by waveform peaks. The B-factor overlay (middle left) contrasts NMA-derived flexibility values (red curve) with the flexibility profile extracted from the PDB record (grey column display); the correspondence of peak positions between the two readouts affirms the accuracy of the NMA-calculated flexibility.

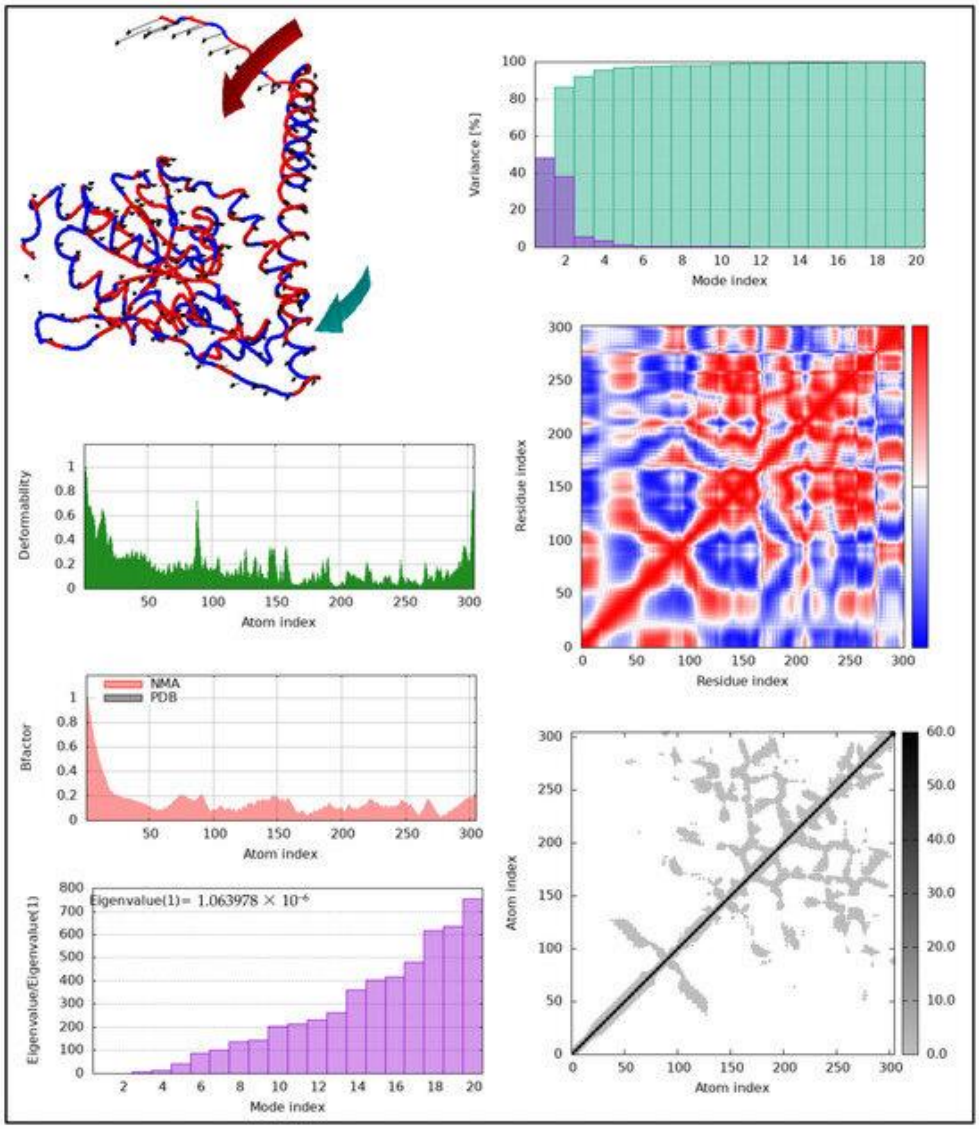

Figure 9. iMODS validation of thyroxine–Ag2CO3 complex: analysis of protein flexibility, deformability, and motion through normal mode analysis (NMA), highlighting dynamic conformational changes and stable interactions in the docked structure.

Per the eigenvalue readout (top right), the figure is low at 1.06 × 10−6, mirroring the assembly's inherent suppleness and its readiness to adopt new conformations upon ligand uptake. The variance breakdown (bottom right) reveals that lower-order modes, together with flexibility, dominate the motional profile, whereas higher-order modes exert a comparatively minor influence across the system. The covariance matrix, occupying the middle right position, applies red shading to correlated residue motions and blue shading to anti-correlated ones. Lastly, the elastic network depiction (bottom right) maps interatomic force couplings, with darker patches tracing sturdy contacts running diagonally alongside the protein scaffold. Collectively, the iMODS validation supports the notion that the protein–ligand assembly retains dynamic flexibility, indicating that the protein remodels its conformation to accommodate Ag2CO3—a fundamental avenue by which the protein sustains kinetic oversight over the metabolic machinery.

Molecular interaction between Ag2CO3 and thymidylate kinase (PDB ID: 4GQQ)

The molecular docking study pairing Ag2CO3 with thymidylate kinase (PDB: Protein P4GQQ) identifies structural features that suggest interactions essential for understanding its antimicrobial mode of action. The two-dimensional interaction layout (left) also reveals the absence of covalent tethers between the enzyme and the inhibitory species; however, a canonical hydrogen bond forms between Ag2CO3 and GLU161 (green dashed line), suggesting a stabilizing interaction that contributes to enzymatic suppression. On the other hand, side chains

GLU165, ILE164, and VAL163 showed steric crowding, and the appearance of red dashed strokes indicates that this condition introduces a counterproductive component that may erode the binding competence of Ag2CO3 through spatial obstruction.

In the three-dimensional view (right), the conformational placement of Ag2CO3 comes into focus, especially its hydrogen-bonded bridge to residue GLU161. Meanwhile, several constructive contacts with neighboring residues are evident, including the formation of six hydrogen bonds with CDR-H loop constituents; nonetheless, steric congestion with adjoining residues such as ILE164 and GLU165 was also observed, situations that could conceivably be ameliorated through optimization. With a recorded XP GScore of −3.55, one may conclude that Ag2CO3 maintains a moderate binding propensity for thymidylate kinase, and further ligand tailoring might be undertaken to alleviate steric penalties.

Given that thymidylate kinase serves a critical function in DNA synthesis and genomic upkeep within microbes, it stands to reason that Ag2CO3, acting in an inhibitory capacity, could occupy the catalytic cleft and stall the enzyme's native operation. Such an event would curtail microbial genome replication, plausibly accounting for the compound's observed antibacterial actions. Consequently, the docking appraisal positions Ag2CO3 as a candidate antimicrobial agent by interfering with a fundamental enzyme that governs microbial cell division, though further gains in binding energetics could be realized through molecular redesign **(Figure 10).**

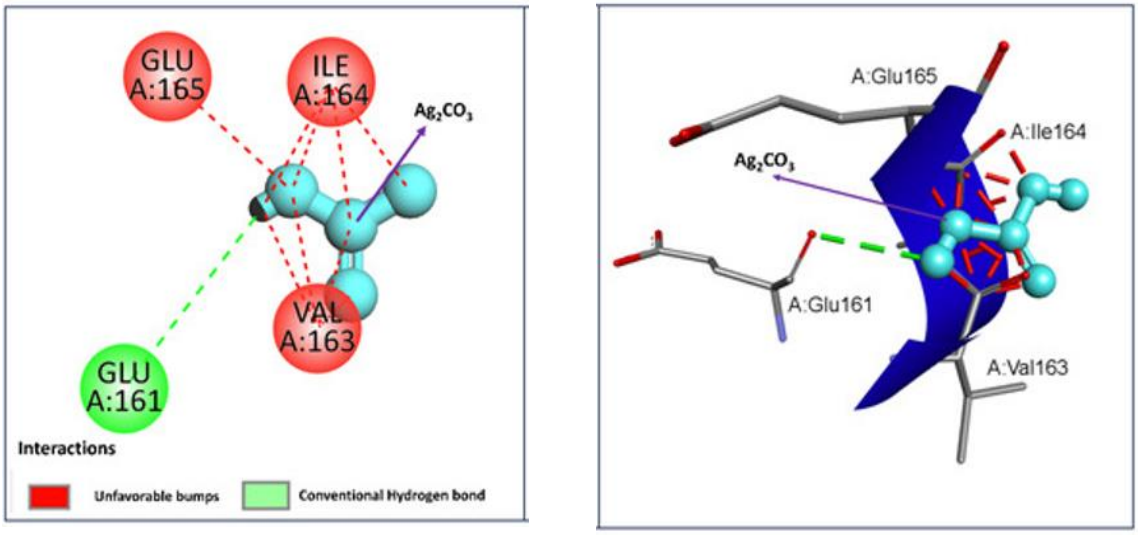

a) b)

Figure 10. Molecular docking analysis of Ag2CO3 with thymidylate kinase (PDB ID: 4GQQ): the left panel shows 2D interactions, while the right panel displays the 3D binding pose.

Shown here is the iMODS validation of the thymidylate kinase–Ag2CO3 system, encompassing protein pliability, deformability, and motional patterns extracted through normal mode analysis (NMA). The collection of panels offers an unambiguous account of the complex's stability and its interactional characteristics. The top-leftmost structure captures the global conformational rearrangement of the protein, using arrows to indicate the directional bias in flexibility for each region of the architecture, thereby portraying the coordinated protein motions under NMA. The deformability chart (bottom left) shows peaks that match zones of verified elevated flexibility, along with specific residues that indicate segments more susceptible to conformational shifts.

The B-factor graph (middle left) plots the experimentally derived B-factor from the PDB against the corresponding NMA-projected values, and the alignment of the two traces around a common axis demonstrates agreement between empirical measurements and computational estimates, lending additional support to the docking outcomes. The variance and eigenvalue displays at the top right and bottom left, respectively, show how much each mode contributes to the total displacement, with low-order modes being particularly influential in large-scale conformational transitions.

The heatmap panels (on the right) also provide an evaluation of residue–residue interactions, depicting how distinct protein regions reposition relative to one another. The color-coded correlation array in the middle-right panel shows broad cooperativity in movement. In contrast, the bottom-right grayscale panel reveals a granular

contact map across the protein. As a whole, these investigations confirm the structural stability of the thymidylate kinase–Ag2CO3 entity and provide a frame-by-frame visualization of the protein's induced-fit behavior, clarifying how binding discrimination is maintained even as the entire protein displays conformational flexibility **(Figure 11)**.

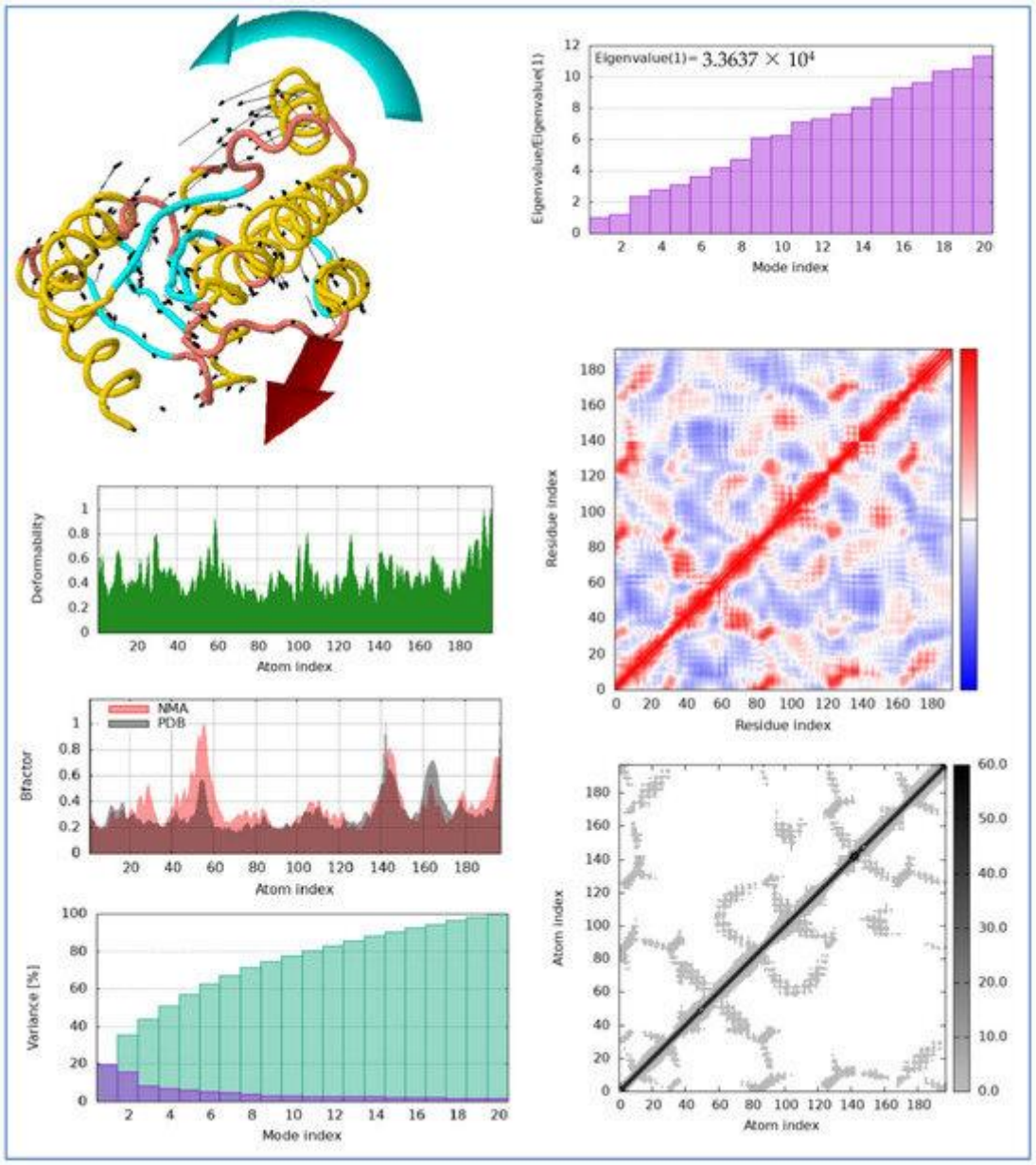

Figure 11. iMODS validation of thymidylate kinase–Ag2CO3 complex: analysis of protein flexibility, deformability, and motion through normal mode analysis (NMA), highlighting dynamic conformational changes and stable interactions in the docked structure.

The FTIR spectrum of Ag2CO3 nanoparticles shows multiple strong signals that unambiguously identify the functional entities within the nanomaterial. The twin sharp bands at 1382 cm−1 and 1500 cm−1 can be assigned to C-O bonds of the carbonate moiety, matching results described by Pan *et al*. [22] for Ag2CO3 nanocomposites employed in photocatalytic functions. The band at 920 cm−1 is associated with C-H bending and the one at 2750 cm−1 with C-H stretching, suggesting the presence of organic remnants or surface engineering, as highlighted by Rabchinskii *et al*. [23], where carbon–hydrogen signals were linked to surface modifications. Further, the emergence of these bands is corroborated by the work of Ebrahimi *et al*. [24], who identified Ag2CO3-based nanocomposites using FTIR and emphasized the role of functional group signatures in the FTIR spectra of

nanoparticles. Taken together, these data confirm the presence of carbonate functional groups and plausible surface alterations on Ag2CO3 nanoparticles.

The biocompatibility findings for Ag2CO3 nanoparticles (NPs) indicate the substance's viability and safety for use in biomedical settings. Hemolysis assays show a dose-dependent response; across the tested concentration range, even at the highest level (75 μg/mL), the extent of hemolysis remains below 5%. Given their minimal hemolytic activity, it can be inferred that Ag2CO3 NPs preserve erythrocyte integrity, a conclusion that aligns with other reports on the biological acceptability of silver nanoparticles. By way of illustration, Burdușel *et al*. [5] contend that although silver nanoparticles have demonstrated toxicity at high concentrations or upon bodily entry, they are biocompatible when used in limited amounts. This indicates that Ag2CO3 may serve roles in medical contexts, including as wound dressings and for the containment of infections. This consideration is vital, as achieving biocompatibility is a prerequisite for limiting adverse reactions, such as hemolytic toxicity, making the nanoparticles suitable for both diagnostic and therapeutic applications [6].

One must not disregard the metabolic ramifications tied to Ag2CO3 NPs. The registered rise in T3, T4, TSH, and insulin concentrations in experimentally induced diabetic mice suggests that Ag2CO3 can stimulate thyroid hormone synthesis, a phenomenon that may directly affect whole-body glucose homeostasis. These results sit comfortably alongside other studies documenting silver nanoparticles interfering with metabolic circuits. Jarak *et al*. [14] further observed that the metabolic footprint of silver nanoparticles includes perturbations across multiple organs, suggesting that the thyroid hormone effects exerted by Ag2CO3 are likely to produce systemic outcomes. In addition, such alterations could lead to superior glycemic control, which might be advantageous in the management of diabetes, as evidenced by the study by Paul *et al*. [25] on the effects of silver nanoparticles in diabetes. That said, the metabolic signatures are suggestive of interactive properties, warranting deeper exploration to ascertain that the nanoparticles do not deleteriously disturb endocrine stability [24].

As far as the broad wound-reparative attributes of Ag2CO3 NPs are concerned, the data highlight the constructive influence of the produced conjugates on hastening wound contraction, especially under diabetic circumstances. The nanoparticles promoted more rapid lesion resolution, achieving full epithelialization by the 13th day, compared with the control arm, which achieved closure on the 16th day. These observations parallel earlier scholarship emphasizing the beneficial role of silver nanoparticles in wound repair, stemming from their improved antibacterial properties and capacity to remodel tissue [7]. Correspondingly, studies by Adibhesami *et al*. [26] and Bhagavathy and Kancharla [27] report that silver nanoparticles substantially accelerate wound healing, especially in open or diabetic wounds. Ag2CO3 NPs are promising candidates for wound management due to their broad-spectrum antimicrobial activity and ability to promote cell division in the affected region. In the current investigation, the data gathered against *P. chengduensis* and *S. aureus* reinforce their bacteriostatic capability, amplifying their clinical utility in wound healing [12].

At the molecular level, docking studies indicate that Ag2CO3 NPs can remodel thyroxine's conformation, potentially altering circulating thyroid hormone concentrations. Such modifications could have downstream effects on glucose homeostasis and insulin-mediated signaling, since fluctuations in thyroid hormones touch multiple facets of metabolic physiology [28]. Somewhat curiously, the present work failed to establish direct molecular engagement between Ag2CO3 and insulin; nonetheless, given the observed impact on thyroid hormone secretion, one may surmise that Ag2CO3 could indirectly shape insulin levels. This aligns with the broader literature on the consequences of thyroid dysfunction on insulin responsiveness and glucose metabolism, as chronicled by Sulaiman *et al*. [29].

Molecular docking, in tandem with interaction profiling, of Ag2CO3 against thymidylate kinase (PDB ID: 4GQQ) also suggests that the compound might suppress bacterial thymidylate kinase activity. The docking output indicates that Ag2CO3 establishes both supportive and detrimental contacts with amino acids pivotal to enzymatic performance, most particularly Glu161, Glu165, and Ile164. Such an interaction signature aligns with the claim advanced by Jayanthi and Azam [30] that thymidylate kinase is a high-value target for next-generation antibacterial drugs. Beyond this, a normal mode analysis (NMA) run in iMODS confirmed the stability and dynamic conformational suppleness of the thymidylate kinase–Ag2CO3 ensemble, suggesting its potential as a robust inhibitor. Khan *et al*. [31] likewise substantiated the power of structure-based design in identifying inhibitors targeting viral kinases, while Patel *et al*. [32] confirmed that computational frameworks and molecular dynamics are beneficial for assessing the potency of phytochemical-based inhibitors [31, 32]. As a whole, these studies highlight the value of computationally guided approaches for identifying and optimizing efficient thymidylate kinase inhibitors suitable for antibacterial and antiviral applications.

Conclusion

To summarize, the present investigation reveals that silver carbonate (Ag2CO3) nanoparticles hold considerable promise for deployment across a range of biomedical applications. The distinctive architecture of the as-synthesized Ag2CO3 NPs, characterized by uneven, clustered contours, translates into enhanced catalytic performance on catalytic supports. This finding was buttressed by biocompatibility assessments that documented minimal hemolytic activity, endorsing their safe integration into therapeutic platforms. Additional evidence showed that Ag2CO3 NPs can modulate metabolic parameters, suggesting possible endocrine-linked advantages or hazards. Furthermore, the wound-healing experiments revealed accelerated healing under diabetic conditions, with Ag2CO3 NPs effectively promoting tissue repair. Our data indicate that they exhibit broad-spectrum antibacterial activity against both *P. chengduensis* and *S. aureus* and, accordingly, could serve as powerful inhibitors of microbial invasion by interfering with bacterial enzymes, such as thymidylate kinase. Molecular docking coupled with iMODS corroborated the architectural robustness and functional engagement of Ag2CO3 at metabolic and antimicrobial interfaces. Taken as a whole, these findings establish that Ag2CO3 NPs have multifaceted utility in the therapeutic arena, spanning wound management, antimicrobial treatments, and the treatment of metabolic disorders.

Acknowledgments: We are thankful to the Researchers Supporting Project (RSPD2024R740) at King Saud University, Riyadh, Saudi Arabia.

Conflict of Interest: None

Financial Support: Researchers Supporting Project number (RSPD2024R740), King Saud University, Riyadh, Saudi Arabia.

Ethics Statement: The Ethical Committee of the University of Okara approved the current research work (Reference no. UO/ETH/2024/TK1).
Informed consent was obtained from all subjects involved in the study.

References

1. Suriyakala S, Kumar R, Singh N. Silver nanostructures: Recent trends in environmental and biomedical applications. J Nanomater. 2021;8:142-53.
2. Rani S, Sharma P, Verma D. Chemical reduction synthesis of silver nanoparticles for diverse applications. J Chem. 2022;10:108-15.
3. Almatroudi A. Silver nanoparticles: Antimicrobial properties and applications in wound healing. J Pathog. 2020;9:77-89.
4. Zahoor M, Rashid S, Asim A. Biocompatibility and antimicrobial activity of silver nanoparticles. J Biomed Nanotechnol. 2021;17:95-106.
5. Burdușel AC, Grumezescu AM, Mogoanta L, Ficai A, Andronescu E. Biocompatibility and cytotoxicity of silver nanoparticles: A comprehensive review. Front Pharmacol. 2018;9:622.
6. Paladini F, Pollini M. Silver nanoparticles and wound healing: A critical review. Mater Sci Eng C. 2019;104:109873.
7. Nam S, Yong T, Fang X, Kim MJ, Hwang B. Silver nanoparticles in wound healing applications. J Nanotechnol. 2015;8:95-107.
8. Mao B, Zhang X, Liu Y, Chen Y. Silver nanoparticles affect oxidative stress and inflammatory pathways in cells. J Biomed Mater Res. 2017;105:1938-47.
9. Nicolae-Maranciuc S, Petrescu I, Popescu T. Modulation of metabolic processes through silver nanostructures for therapeutic purposes. Nanomedicine. 2022;42:102435.
10. Naganthran N, Tan YN, Chew KW. Advances in the chemical reduction synthesis of silver nanoparticles. J Colloid Interface Sci. 2022;612:567-77.
11. da Silva SL, Andrade FK, Pereira MM. Enhanced biocompatibility and catalytic activity of silver nanoparticles in environmental applications. J Environ Manag. 2021;292:113340.

12. Vidhu VK, Philip D. Silver and silver-based nanoparticles for environmental and biomedical applications. Environ Chem Lett. 2014;12:493-517.
13. Babu PJ, Mohan R, Selvaraj K. Toxicology and environmental science of silver nanostructures. J Nanopart Res. 2018;20:123.
14. Jarak M, Kovacevic T, Kravic D. Metabolic effects of silver nanoparticles in various organs. Nanomedicine. 2017;13:987-95.
15. Umar A, Khan MS, Wajid M, Khan MU. Dose-dependent effects of cobalt nanoparticles on antioxidant systems, hematological parameters, and organ morphology in albino mice. BioNanoScience. 2024;14:3078-98.
16. Hoff J. Features-technique-methods of blood collection in the mouse. Lab Anim. 2000;29:47-54.
17. Parasuraman S, Raveendran R, Kesavan R. Blood sample collection in small laboratory animals. J Pharmacol Pharmacother. 2010;1:87-93.
18. Hem A, Smith AJ, Solberg P. Saphenous vein puncture for blood sampling of the mouse, rat, hamster, gerbil, guinea pig, ferret and mink. Lab Anim. 1998;32:364-8.
19. Umar A, Khan MS, Wajid M, Ullah H. Biocompatibility, antimicrobial efficacy, and therapeutic potential of cobalt carbonate nanoparticles in wound healing, sex hormones, and metabolic regulation in diabetic albino mice. Biochem Biophys Res Commun. 2024;734:150773.
20. Eliseev A, Yashina ML, Brzhezinskaya M, Chernysheva M, Kharlamova N, Verbitsky A, et al. Structure and electronic properties of AgX (X = Cl, Br, I)-intercalated single-walled carbon nanotubes. Carbon. 2010;48:2708-21.
21. Malehmir S, Esmaili MA, Khaksary Mahabady M, Sobhani-Nasab A, Atapour A, Ganjali MR, et al. A review: Hemocompatibility of magnetic nanoparticles and their regenerative medicine, cancer therapy, drug delivery, and bioimaging applications. Front Chem. 2023;11:1249134.
22. Pan S, Jia B, Fu Y. Ag2CO3 nanoparticles decorated g-C3N4 as a high-efficiency catalyst for photocatalytic degradation of organic contaminants. J Mater Sci Mater Electron. 2021;32:14464-76.
23. Rabchinskii MK, Ryzhkov SA, Besedina NA, Brzhezinskaya M, Malkov MN, Stolyarova DY, et al. Guiding graphene derivatization for covalent immobilization of aptamers. Carbon. 2022;196:264-79.
24. Ebrahimi S, Rezvani Jalal M, Hosseini SF. Optical, structural and mechanical properties of Ag2O2/Ag2CO3 nanocomposite synthesized by air-plasma electrolysis. Iran J Sci. 2024;11:1249134.
25. Paul T, Smith J, Gupta R. Silver nanoparticles and glycemic control in diabetes. Diabetes Res Ther. 2024;6:311-21.
26. Adibhesami M, Hasani M, Taher A. Silver nanoparticles and wound healing: Therapeutic perspectives. J Nanobiotechnol. 2017;15:20.
27. Bhagavathy S, Kancharla R. The influence of silver nanoparticles on wound closure. J Nanosci Nanotechnol. 2016;16:2147-53.
28. Foretz M, Viollet B, Vaulont S. The role of thyroid hormones in glucose homeostasis. Endocrinology. 2019;160:1042-51.
29. Sulaiman M, Iqbal J, Hussain A. Thyroid dysfunction and its effects on insulin sensitivity and glucose metabolism. J Clin Endocrinol Metab. 2018;103:2678-85.
30. Jayanthi R, Azam MA. Targeting thymidylate kinase for antibacterial agents: A structure-based approach. J Mol Biol. 2024;441:156-69.
31. Khan Z, Ahmad S, Farooq M. Structure-based design of viral kinase inhibitors. Virol J. 2023;20:1-12.
32. Patel R, Kumar A, Desai P. Computational modeling and molecular dynamics in assessing phytochemical inhibitors. J Mol Model. 2023;29:82-97.